The helix wake and its properties: reduced order modeling through dynamic mode decomposition

Claudia Muscari[1,3], Paolo Schito[1], Axelle Viré[2], Alberto Zasso[1], and Jan-Willem van Wingerden[3]

[1]Politecnico di Milano
[2]Delft University of Technology, Faculty of Aerospace Engineering, Kluyverweg 1, 2629HS Delft, The Netherlands
[3]Delft University of Technology, Delft Center for Systems and Control, Mekelweg 2, 2628 CD Delft, the Netherlands

Correspondence: Claudia Muscari (claudia.muscari94@gmail.com)

Abstract. Wind turbine wakes can be treated as a complex system of helical vortices. When this system destabilizes, the wake recovers its velocity deficit through mixing and entertainment of energy from the surrounding flow. How fast and effectively that happens depends on the inflow characteristics and can also be influenced by how the turbines are operated. Dynamic induction control techniques such as the helix affect the onset of instability and the transition from near to far wake, but the exact mechanisms are still unclear. Its potential in a wind farm context has been proved both numerically and experimentally, but a helix wake model does not exist yet. The goal of this study is to derive a data-driven model of the helix wake and characterize it. Dynamic mode decomposition of data generated with large eddy simulations is performed. We simulate the DTU 10 MW model turbine under a range of helix excitation frequencies and different inflows. We show that the helix modes are dominantly present both in laminar and turbulent flow. However, as turbulence intensity increases, they exhibit larger spatial decay and temporal amplitude. Additionally, we identify inflow modes related to the turbulence length scales of the inflow. We show that a very limited number of modes allows us to reconstruct the initial flow field accurately and that the optimum excitation frequency for the control technique depends on the turbulence intensity and on the position of the downstream turbines.

1 Introduction

In the last few decades, the transition to renewable sources of energy has emerged as critical to the survival of our species on this planet. Climate change is currently the biggest threat to our societies and has already caused irreparable damage to the biosphere. Wind is a clean and abundant resource, and the technology to harness it is mature and competitive. The wind energy industry is the fastest-growing one in the renewables landscape, with big, ambitious projects being developed all over the globe (IEA, 2023). Although wind is abundant, favorable locations for wind turbines are not. A proper location should not only have strong, uniform wind but also be far enough from inhabited centers and respond to logistic necessities related to transport, installation, maintenance, and connection to the grid. In this context, the strategic arrangement and clustering of wind turbines into farms play a pivotal role in maximizing efficiency (Akhmatov and Knudsen, 2002). When a farm perspective is adopted, wake aerodynamics becomes extremely relevant to the turbine's operation and control. The wake of a wind turbine is an area of flow characterized by lower velocity and higher turbulence intensity that extends for several diameters downstream of the turbine itself. When wind turbines are placed in clusters, the downstream turbines will easily operate in the wake of the

25 upstream ones, with lower energy available for extraction and increased fatigue loads. This ultimately impacts the turbines'
power production and their life span (Lee et al., 2012).

Wind farm control (WFC) is the branch of wind energy that studies how a certain behavior of the wind farm can be achieved
from a global perspective. This means that certain turbines will perform sub-optimally but that the gain for the whole farm
exceeds the individual loss. The objectives of WFC are load mitigation and power maximization. Most research focuses on
30 the latter (Meyers et al., 2022). The two concepts currently dominating the field are based on wake redirection (WR, Fleming
et al., 2015) and dynamic induction (Munters and Meyers, 2018). The first mainly relies on misaligning the rotor with the
incoming wind direction by static yaw control. It made a first appearance in Clayton and Filby (1982), was then extensively
tested numerically (Jiménez et al., 2010; Gebraad et al., 2016), on model turbines (Campagnolo et al., 2020) and on the field
(Doekemeijer et al., 2021) and is now officially on the market (Siemens Gamesa, 2019). Dynamic induction control (DIC) is
35 more recent and is at a different development stage. The main difference with WR (at least in its most common variant) is
that dynamic control techniques have the ambition of not only adapting the turbine set-points to changes in wind direction
and/or speed but rather actively affecting wake mixing and turbulence. The DIC techniques dominating the field are the pulse
(Munters and Meyers, 2018) and the helix (Frederik et al., 2020). In both cases, induction control is achieved by means of
pitch actuation: collective for the pulse and individual for the helix. Recently, a lot of effort has gone into explaining how
40 DIC affects the onset of instability and the transition from near to far wake. Croce et al. (2023) suggested that the quicker
wake re-energization through DIC techniques should be attributed to the anticipation of vortex roll-up, which occurs when the
boundary layer rolls around higher vorticity cores. In Hodgkin et al. (2023), the authors concluded that, in a fully turbulent
atmospheric boundary layer (ABL) inflow, this might not be the case as the breakdown of tip vortices comes from a complex
interaction across a range of excitation frequencies. Korb et al. (2023) performed a thorough characterization and observed
45 that the pairing and leapfrogging of vortices are not visible when a varying blade pitch is applied since the thickening and
shrinking of the tip vortices rather lead to their merging. They also questioned the attribution of the power gains obtainable
with the helix to the sole early wake mixing and separated the contribution of meandering, deflection, and deformation. In
the aforementioned studies, wake instabilities were predicted through linear stability analysis: the Navier-Stokes equations
were linearized around the base flow, and small perturbations were introduced to analyze their spatial and temporal evolution.
50 An alternative approach consists of taking time-resolved data from experiments or numerical simulations and applying modal
decomposition techniques. Some of these techniques were first developed for applications to fluid dynamics (Schmid, 2010)
and have been recently applied to wind turbines' and propellers' wakes (Sarmast et al., 2014). Sarmast et al. (2014) focused
on the mutual inductance instability of the wake, using both proper orthogonal decomposition (POD) and dynamic mode
decomposition (DMD) and deriving a model for determining the stable wake length. Magionesi et al. (2018) applied POD and
55 DMD to the wake past a marine propeller and found modes related to the coupling of tip vortices, hub-tip vortex interaction,
and wake meandering. Despite their popularity, data-driven approaches such as POD and DMD have not yet been widely
applied to dynamically manipulated wakes. Understanding the mechanisms that make dynamic induction control effective in
anticipating wake breakdown would benefit enormously from both the identification of dominant coherent structures and the
availability of reduced order models (ROMs). Muscari et al. (2022, 2023) is the first example of a data-driven approach to

the modeling of helicoidal wakes: large eddy simulations (LES) data of standard, pulsatile, and helicoidal wakes was fed to a physics-informed DMD (pi-DMD) algorithm to obtain the dominant dynamic modes in these configurations. Since the inflow was uniform, the resulting dominant modes were very clearly related to the DIC strategy adopted. In particular, the dominant modes were associated to the same Strouhal number of the helix excitation signal and its harmonics. The Strouhal number, $St = fD/u_\infty$, where f is the dominant frequency, D is a length scale (the turbine rotor diameter in our case), and u_∞ is the freestream velocity, is a dimensionless quantity often used to represent periodic flow mechanisms. We know that higher turbulence intensity of the inflow leads to faster wake recovery. In fact, inflow turbulence intensity influences the length of the near-wake and the persistence of tip vortices. With more realistic inflows, we expect the role of DIC to be smaller in the wake recovery compared to the inflow turbulence. However, how the DMD modes will change and whether they are still relevant in the wake dynamics remains an open question. The first contribution of this work is to derive a simple model for helicoidal wakes under turbulent inflow and use it to give an answer to this question.

While DMD is guaranteed to give us valuable information on the physics of the helix, some fundamental questions on wake dynamics remain open. One example is the nature of wake meandering, a low-frequency, large-scale lateral motion of the wake. Recent studies have shown that inflow turbulence and periodic perturbations (such as those introduced with DIC) interact in a complex way. Mao and Sørensen (2018) performed a non-linear optimal perturbation analysis of the wake downstream of an actuator disk. They found that the optimal perturbation had the shape of an azimuthal wave in the stream-wise direction with a frequency corresponding to a $St = 0.25$. The value found in Mao and Sørensen (2018) is in the range of frequencies considered optimal for DIC (Munters and Meyers, 2018). Forcing at this frequency led to substantial amplification of the inflow perturbation in the wake flow. Some of these studies reinforce the view of meandering as an intrinsic property of the wake flow triggered by the selective amplification of upstream disturbance. The presented view of the phenomenon contradicts the assumption at the basis of the Dynamic wake meandering (DWM) model (Larsen et al., 2008), which assumes that the wake acts as a passive tracer advected downstream by the mean wind. Lin and Porté-Agel (2024) simulated an array of eight NREL 5MW (Jonkman et al., 2009) wind turbines where the first turbine was undergoing sinusoidal yaw control. The inflow had a 8% stream-wise turbulence intensity. The main finding was that the optimal power gain was obtained when the dynamic yawing triggered meandering resonance. Interestingly, similar results are shown in Li et al. (2022) for a floating offshore wind turbine (FOWT), where side-by-side motions triggered the meandering resonance. Hodgson et al. (2023) studied the inflow turbulent time scales' effect on wake recovery, isolating their influence from the other properties such as turbulence kinetic energy, buoyancy, and shear. They found that a certain range of inflow Strouhal numbers (0.33-0.66) consistently results in the greatest amplification of stream-wise velocity fluctuations, regardless of whether this was the dominant component of the inflow. In light of these results, the second contribution of this work is to explore if and how the helix interacts with inflow perturbations.

In this paper, we present a data-driven analysis of helicoidal wakes under uniform and turbulent inflow conditions and provide insight into the contribution of DIC to the wake dynamics. The data is gathered through LES and a wake model is derived with DMD. We verify that DMD modes related to pitch excitation remain dominant when turbulence is introduced and show that a ROM of a helicoidal wake could be built out of as few as two modes. We demonstrate that the optimal excitation

frequency is a function of the inflow and the position downstream, contrary to what was initially thought for DIC (Munters and Meyers, 2018). The paper structure is the following: Section 2 briefly presents the theory behind the helix and DMD, Section 3 details the flow and wind turbine models adopted and describes the setup. In Section 4, we show the obtained dynamic modes and elaborate on how turbulence affects the wake physics and the efficacy of DIC. Finally, we summarize our main conclusions and elaborate on possible further steps in Section 5.

2 Methodology

This section describes the helix, gives a general theoretical overview of modal decomposition techniques, and presents the DMD algorithm used for this work.

2.1 The helix

The helix (Frederik et al., 2020) uses individual pitch control (IPC) to dynamically manipulate the wind turbine wake with lower power production and wake velocity fluctuations compared to other DIC strategies. The pitch angles of the blades vary with sinusoidal signals that have the same (low) frequency and amplitude with a phase offset. This results in yaw and tilt moments on the rotor that force wake meandering. The resulting velocity field is helicoidal, hence the name of the strategy. If the phase offset between tilt and yaw angles is equal to $\pi/2$, the helix rotates in a counterclock-wise (CCW) direction; if it is equal to $3/2\pi$, the helix rotates in a clock-wise (CW) direction. In practice, the desired pitch signals in a rotating reference frame θ_b (one for each blade b), can be obtained with an inverse multi-blade coordinate (MBC) transformation T^{-1}, as follows:

$$\begin{bmatrix} \theta_1(t) \\ \theta_2(t) \\ \theta_3(t) \end{bmatrix} = T^{-1}(\Psi) \begin{bmatrix} \theta_0(t) \\ \theta_{tilt}(t) \\ \theta_{yaw}(t) \end{bmatrix}, \tag{1}$$

with

$$T^{-1}(\psi) = \begin{bmatrix} 1 & cos(\psi_1) & sin(\psi_1) \\ 1 & cos(\psi_2) & sin(\psi_2) \\ 1 & cos(\psi_3) & sin(\psi_3) \end{bmatrix}, \tag{2}$$

where the angle ψ_b is the azimuth angle for blade b, and θ_0 is the fixed-frame collective pitch. Finally:

$$\theta_b(t) = \begin{bmatrix} 1 & cos(\psi_b) & sin(\psi_b) \end{bmatrix} \begin{bmatrix} \theta_0(t) \\ \theta_{tilt}(t) \\ \theta_{yaw}(t) \end{bmatrix} = sin[(\omega_r + \omega_e)t + \psi_{0,b}], \tag{3}$$

where ω_r is the rotational velocity and ω_e is the one relative to the pitch excitation. For this study, these equations were embedded in the SOWFA supercontroller (Fleming et al., 2013).
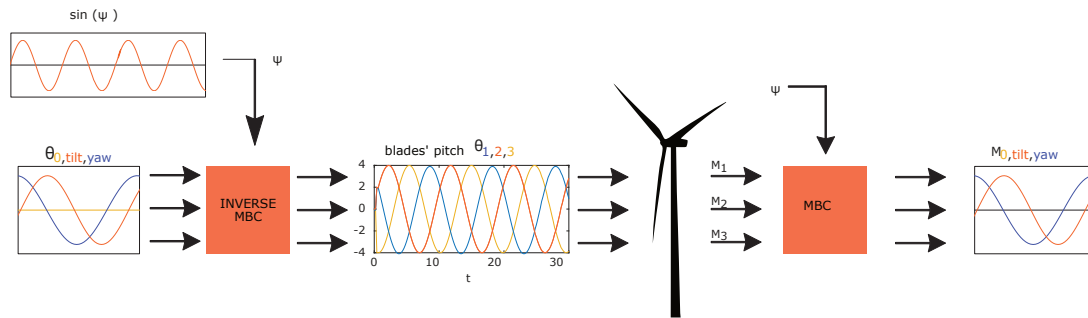
Figure 1. Schematic representation of how the multi-blade coordinate transformation is used to obtain a directional thrust force.

2.2 Modal decomposition

Wind turbine wakes can be described as high-dimensional, nonlinear dynamical systems characterized by multi-scale phe-
nomena in both space and time. However complex, they often exhibit low-dimensional behavior. This makes modal analysis
techniques a very attractive option to address the complex dynamics of wakes. These techniques are data-driven, and the
philosophy behind them, in general, is to reduce the order of the problem by projecting high-dimensional data onto a lower-
dimensional space. This allows the extraction of coherent spatio-temporal structures that represent the system with a number
of modes that is orders of magnitude smaller than its state dimension.

Among the various techniques, one that first emerged in the field of fluid mechanics is proper orthogonal decomposition
(POD). POD determines spatial modes, which are ordered according to their energy content. It was first applied to fluid
dynamics by Lumley J.L. (1967). Starting from the data, we can build a matrix of snapshots, each representing the system's
state of interest at a given time. We normally assume that the snapshots are spaced equally in the evolution direction and that
the total spatial dimension is higher than the number of snapshots (the matrix is tall and skinny). We can take the snapshot
matrix and break it down into three matrices. The first contains the modes and gives us spatial information; the second gives
us the mode amplitude; the third contains time information and allows us to reconstruct the dynamics. If we enforce the first
matrix's orthogonality and the second's diagonality, the transformation applied is a singular value decomposition (SVD), and
the modes obtained are the POD modes. Disadvantages of POD are that:

- it is sensitive to outliers;

- spacial orthogonality is not always physically significant;

- ordering by energy is not always appropriate;

- temporal dynamics is multi-frequential.

In Rowley et al. (2009), dynamic mode decomposition (DMD) was introduced. It is also a data-driven approach; however,
unlike POD, it produces modes based on their dynamics rather than the energy content and is characterized by a single fre-
quency. The signal is split into a triplet of purely spatial modes, scalar amplitudes, and purely temporal signals. This makes it

more suitable for the identification of dominant frequencies. Its applications to fluid dynamics in general and wind energy, in particular, include diagnostic and future state prediction. Various DMD algorithms have been developed and used for pattern detection (Schmid, 2022), reduced order models (ROMs) extraction (Alla and Kutz, 2017), and control (Cassamo and van Wingerden, 2021).

2.2.1 Exact DMD algorithm

Dynamic mode decomposition (DMD) is a powerful tool for tackling complex dynamical systems, particularly in domains like fluid dynamics. However, the standard algorithm has certain significant drawbacks, like susceptibility to noise and a tendency to over-fit. For this reason, many variants of the algorithm have been proposed in the literature (Schmid, 2022). The variant we used in this paper is exact DMD (Tu, 2013), which solves the issues of the standard algorithm without adding complications.

The DMD algorithm takes as input a number m of snapshots of the flow field. These snapshots can be obtained both experimentally and numerically, and they represent the state of the considered system at a certain time step. As a first step, the snapshots should be shaped into very tall columns. In our case, they will be organized as follows:

$$x_k = \begin{bmatrix} u(t_k)^T & v(t_k)^T & w(t_k)^T \end{bmatrix}^T \in \mathbb{R}^{n \times 1}, \tag{4}$$

where $u(t_k), v(t_k), w(t_k)$ represent the vectorized velocity fields in the 3 dimensions at time instant t_k.

The series of snapshots is assembled into two matrices X and X':

$$X = \begin{bmatrix} x_1 & x_2 & x_3 & \dots & x_{m-1} \end{bmatrix} \in \mathbb{R}^{n \times m-1}, \quad X' = \begin{bmatrix} x_2 & x_3 & x_4 & \dots & x_m \end{bmatrix} \in \mathbb{R}^{n \times m-1}, \tag{5}$$

with $n \in \mathbb{Z}^+$ being the state dimension and $m \in \mathbb{Z}^+$ being the number of snapshots.

DMD aims to find the best linear operator A that advances X into X'.

$$X' \approx AX \qquad (x_{k+1} = Ax_k). \tag{6}$$

The DMD problem can then be formulated as:

$$\underset{rank(A)=r}{\operatorname{argmin}} \|X' - AX\|_F, \tag{7}$$

where $\| * \|_F$ is the Frobenius norm.

When the state dimension n is very large, it is unfeasible to deal with the full $A \in \mathbb{R}^{n \times n}$ matrix directly. The DMD algorithm substitutes it with a POD-projected matrix $\widetilde{A} \in \mathbb{R}^{r \times r}$ with r the reduced state dimension. This matrix is obtained using the Singular Value Decomposition (SVD) of X

$$X \approx U\Sigma V^*, \tag{8}$$

where $*$ denotes the complex conjugate transpose, $U \in \mathbb{C}^{n \times r}$, $\Sigma \in \mathbb{C}^{r \times r}$ and $V \in \mathbb{C}^{m \times r}$. The left singular vectors **U** are POD modes. The columns of **U** are orthogonal, so $U^*U = I$; similarly $V^*V = I$. The matrix $\widetilde{A}$ can thus be written as

$$\widetilde{A} = U^*AU = U^*X'V\Sigma^{-1}. \tag{9}$$

The following step is the eigen-decomposition of $\widetilde{A}$:

$$\widetilde{A}W = W\Lambda, \tag{10}$$

where the columns of $W \in \mathbb{C}^{r \times r}$ are eigen-vectors and $\Lambda \in \mathbb{C}^{r \times r}$ is a diagonal matrix containing the corresponding eigenvalues $\lambda_k \in \mathbb{C}$. As anticipated, we now have the spatial modes (eigenvectors) and their growth/decay rates and oscillation frequencies (from the eigenvalues).

3   Numerical environment

This section presents the numerical models adopted and the simulation setups.

3.1   Inflow model

The atmospheric boundary layer (ABL) is simulated with SOWFA (Churchfield et al., 2012a). SOWFA is based on OpenFOAM (Jasak, 2009), an open-source CFD code that discretizes the Navier-Stokes equations. The representation of the rotor, described in Section 3.2, is non-geometric and does not require a very fine grid around the blades. This allows us to perform LES by avoiding their issues with the treatment of near-wall regions (Rodi et al., 1997). At the same time, the computational cost is maintained low. When using LES, the larger turbulent scales are simulated, while the effect of the smaller ones (the viscous subrange) is mimicked with a sub-filter-scale model. In particular, SOWFA uses a one Equation Eddy Viscosity Model for incompressible atmospheric flows. The model is based on the original *oneEqEddy* OpenFOAM model (Greenshields et al., 2018), but has some small modifications, such as buoyancy production, specific to atmospheric flow. Turbulent initial conditions are introduced by running precursor simulations with the atmospheric *ABL solver*. The solver allows the user to specify surface roughness, stability, wind speed, and direction. Precursor simulations are performed in a domain without the wind turbine over a time span that is sufficient for the turbulence to develop correctly. The volume field is then used to initialize the wind farm simulation (successor), and data planes are used as inflow boundary conditions.

3.2   Turbine Model

The rotor is modeled with the actuator line model (ALM, Sorensen and Shen, 2002). When considering wind turbines, the large Reynolds numbers and the multiple length scales involved make LES on a fully resolved geometry too computationally demanding to be used extensively. For this reason, hybrid methods compute the effect of the turbine on the flow analytically. ALM is an improved version of the popular actuator disk model (ADM), which is a direct descendant of Glauert's Blade Element Momentum (Glauert, 1963). With the ALM, forces exchanged between the flow and the blades are computed along lines that correspond to the individual blades. Velocities are sampled from the computational domain, and the aerodynamic coefficients are obtained from polar data. Once obtained, the forces are smeared over several cells to prevent numerical issues. Additionally, with the ALM, blades can be modeled in a way that allows them to respond dynamically to changing conditions and can account for aeroelasticity when coupled to a structural code. This allows us to describe the wake's dynamics better

200 (with respect to ADM) and capture the tip vortices (provided that the resolution is sufficient) and their influence on the induced velocities. However, smaller-scale phenomena, such as those involving the blade boundary layer, cannot be captured.

3.3 Setup

The following is a description of the setup of the LES cases used to build the data set. All of the simulations have one of the three setups described below.

205 ### 3.3.1 Space Discretization

For all cases, the domain is a $2.5 \times 1 \times 0.6$ km box with the specific discretization reported in Table 1 and the refinement areas illustrated in Figures 2 and 3. The uniform case discretization is the same as in Muscari et al. (2022), as the same data set was used. The precursor mesh does not need a fine resolution: the turbine is not in the domain, and we just want the selected turbulent conditions to develop. Based on the literature (Churchfield et al., 2012b), the resolution required for that to happen

210 is in the order of 10 m. The selected dimension of a precursor cell is 12.5 m. This base mesh required only two refinements for the successor cases to reach the same resolution of the uniform ones away from the walls. Each refinement halves the characteristic dimension of the cell so that we get to $\Delta x = 3.125$ m in the rotor area. The considered rotor is the DTU 10 MW reference turbine (Bak et al., 2013), which has a diameter of $D = 178.3$ m. For all turbine simulations, $D/\Delta x = 58$. While, according to Churchfield et al. (2012a), $D/\Delta x = 50$ should be sufficient, in our case we do not properly captures the smaller

215 structures in the wake (see 5). This limit was dictated by our computational resources and should be addressed in future works.

Table 1. Mesh characteristics for the three types of simulations.

	domain extension			number of cells			number of refinements	smallest cell dimension
	x	y	z	x	y	z		
uniform case	2500 m	1000 m	600 m	50	20	12	4	3.125 m
precursor	2500 m	1000 m	600 m	200	80	48	0	12.5 m
successor	2500 m	1000 m	600 m	200	80	48	2	3.125 m
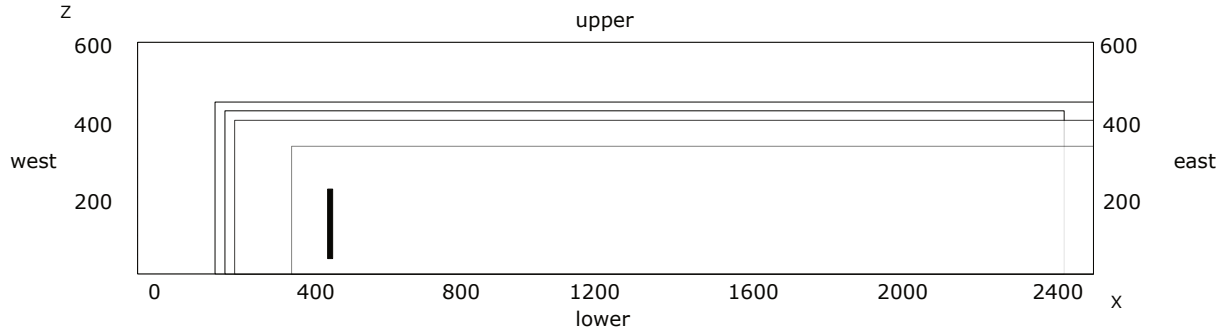
Figure 2. Vertical slice of the domain in the uniform case, showing where the refinement zones are positioned and how the boundaries are indicated. The rotor is represented by the thick black line.
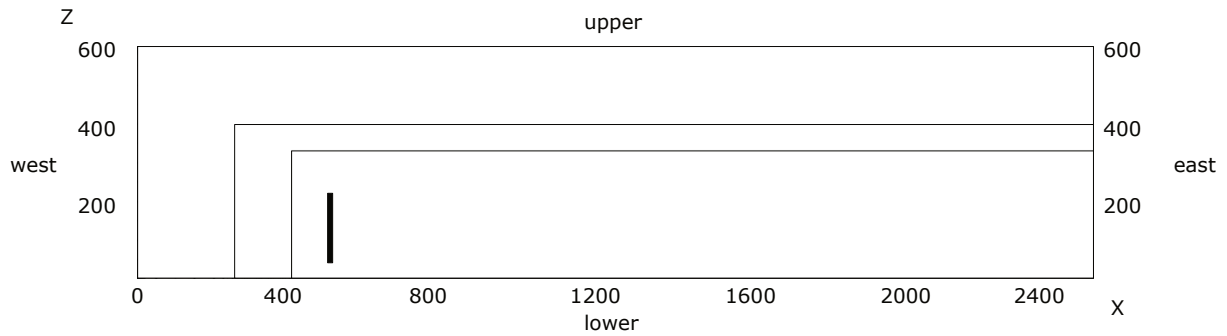
Figure 3. Vertical slice of the domain in the successor case, showing where the refinement zones are positioned and how the boundaries are indicated. The rotor is represented by the thick black line.

3.3.2 Time Discretization

For the uniform case, the total simulated time is 3000 s, but for the DMD snapshots, we discarded the transient part, corresponding to the initial 1400 s. The simulation time step is 0.2 s, and a snapshot is taken once every 2 s. Our computational resources downwardly limited the time step. It respects the standard Courant–Friedrichs–Lewy (CFL) condition but not the more stringent one normally required for actuator line simulations. The condition is formulated in Equation 11 and it indicates that the tip of the blade should not cross more than a cell over a time step.

$$CFL_{tip} = \frac{\omega R \Delta t}{\Delta_g} < 1 \tag{11}$$

where ω is the wind turbine rotational speed, R is the blade radius and $\Delta_g = \sqrt[3]{\Delta_x \Delta_y \Delta_z}$ is the equivalent cell dimension. In our case $CFL_{mean} = 0.25$ and $CFL_{tip} = 10$. We deem this to be acceptable since we are not properly modeling the tip-vortices anyway. The precursor needs to run for a long time before the data planes for the successor can be sampled. The total duration of our precursor was 33000 s with a time step of 0.5 s .

3.3.3 Initial and Boundary Conditions

The domain boundaries are reported in Table 2 and Table 3, together with the assigned boundary conditions for the main quantities. The turbine is located 500 m downstream of the inlet and in the middle between the north and south walls. Some of the boundary conditions might require further explanation. With *fixed flux pressure*, the pressure gradient is set in a way such that the velocity boundary condition specifies the flux on the boundary. The *inletOutlet* condition is equivalent to the *zero gradient* one, but it switches to a *fixed value* in case of backward flow.

Table 2. Boundary conditions for the precursor

patch	U	p	T	k	nu
lower	ABL wall function	fixed flux	zero gradient	zero gradient	fixed value
upper	slip	fixed flux	fixed gradient	zero gradient	fixed value
west	cyclic	cyclic	cyclic	cyclic	cyclic
east	cyclic	cyclic	cyclic	cyclic	cyclic
north	cyclic	cyclic	cyclic	cyclic	cyclic
south	cyclic	cyclic	cyclic	cyclic	cyclic

Table 3. Boundary conditions for the successor

patch	U	p_{rgh}	T	k	nu
lower	ABL wall function	fixed flux pressure	zero gradient	zero gradient	fixed value
upper	slip	fixed flux pressure	fixed gradient	zero gradient	fixed value
west	time varying mapped fixed value	fixed flux pressure	time var. mapped fixed value	time var. mapped fixed value	zero gradient
east	inletOutlet	zero gradient	zero gradient	zero gradient	zero gradient
north	inletOutlet	fixed flux pressure	zero gradient	zero gradient	zero gradient
south	inletOutlet	fixed flux pressure	time var. mapped fixed value	time var. mapped fixed value	zero gradient

For this study, two precursors were considered. The simulated ABL is neutral in both cases, meaning that shear is the dominant phenomenon, and the parameter affecting the turbulence the most is the roughness length z_0. The velocity is controlled through a uniform pressure gradient such that the wind speed at hub height is 9 m/s. The inflow wind profile is logarithmic, and the potential temperature is set using a capping inversion width of 100 m, a reference potential temperature of 300 K, an initial capping inversion height of 750 m, a potential temperature jump across the capping inversion of 5 K and a stable lapse rate of 3 K/km. Turbulence is triggered using sinusoidal spanwise velocity perturbations in the first 100 m of the ABL. The Coriolis parameter is set to $4.813 \cdot 10^{-5}$ rad/s, corresponding to a latitude of $41.44°$. The main ABL parameters are summarized in Table 4. As turbulence is developed inside the ABL, the velocity controller slowly rotates the wind direction at geostrophic height, trying to maintain the desired magnitude and direction at the reference height. After 30000 s, the ABL height is kept constant, and turbulence statistics can be computed (see Figure 4).

Table 4. Main ABL parameters for the precursor simulations

u_{ref}[m/s]	h_{ref}[m]	θ_0 [K]	Δ_h [m]	γ[K/km]	$H_{inversion}$ [m]	f_c [rad/s]	$z_{0,TI=3.3\%}$	$z_{0,TI=6.5\%}$
9	115	300	100	3	750	$4.813 \cdot 10^{-5}$	10^{-6}	10^{-2}

Our choices resulted in a mean turbulence intensity (TI) at the hub height of 3.3% in one case and 6.5% in the other. These values are representative of the range of TI that a first-row wind turbine can experience when placed offshore. The tower is about 115 m, meaning the turbine will partially operate outside the Prandtl layer.
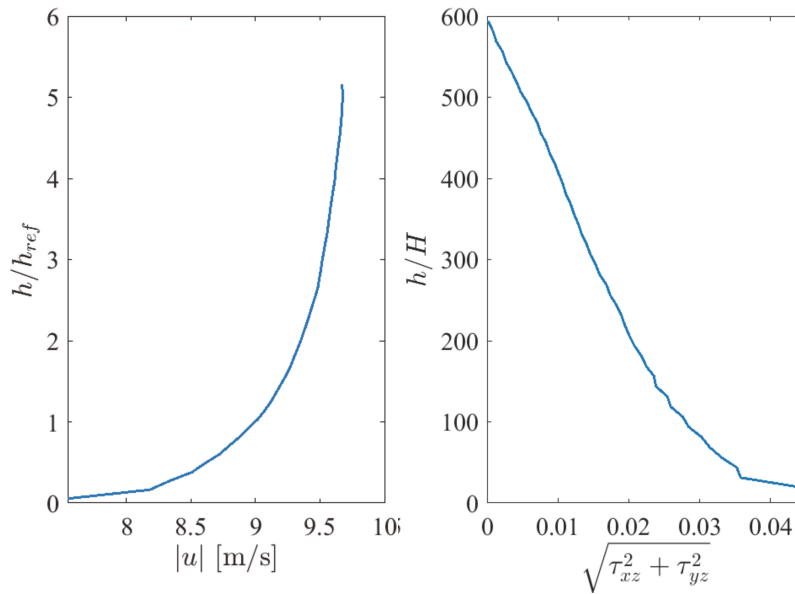
Figure 4. Precursor stream-wise velocity and shear stress profiles.

In the final hundred seconds of the precursors' simulations, we collected velocity data from a diameter-long vertical line of probes through the point where the hub should be and on a horizontal line from the same point in the stream-wise direction to the end of the domain. We used these data to estimate the turbulence integral length scales in these directions. The definition of the integral length scale, L, that we adopted is based on Taylor's hypothesis on frozen turbulence. With this assumption, the integral length scale at a certain position can be expressed as a function of an integral time scale at that position:

$$L(z) = U(z) \cdot T(z) \tag{12}$$

This integral time scale is calculated as follows:

$$T = \int\limits_{0}^{1/e} \rho(\tau) \cdot d\tau \tag{13}$$

where $\rho(\tau)$ is the auto-correlation coefficient of the time signal of the velocity fluctuations, and e is Euler's number. Table 5
255 summarizes the results:

Table 5. Mean turbulence length scale in vertical and stream-wise direction in correspondence of where the hub of the turbine would be

TI	$\overline{L_x}$[m]	$\overline{L_z}$[m]
3.3%	345	268
6.5%	387	274

4 Results

This study includes results from a total of 23 simulations, including 2 precursor simulations. The setup is as described in Section 3.3. In each of the simulations, we have a single DTU 10 MW turbine controlled with a CCW helix with amplitude $4°$ and frequency varying in the range $St \in [0.15, 0.2, 0.25, 0.3, 0.35, 0.4]$. This is done for three different inflow conditions: a
260 uniform inflow and turbulent inflows with $TI = 3.3\%$ and $TI = 6.5\%$.

4.1 Wake Deficit Recovery

In this Section, before going into the DMD analysis, we look at instantaneous flow-field results and at the evolution of normalized global quantities in the wake. Figures 5 and 6 show a top view of the wake, for the low turbulence case, at the last step of the simulation with a comparison between baseline and helix control with $St_{exc} = 0.4$. We only show this case because it
265 allows a clearer visualization of what happens in all cases, including the high turbulence ones. In particular, Figure 5 shows the stream-wise velocity, u, normalized by the value imposed at the rotor hub ($9 \, \mathrm{m/s}$), and Figure 6 shows the vertical component of the velocity, v, on a same vertical plane passing through the hub.

We can clearly observe an earlier onset of instability in the cases where the helix control is used. We see it, in particular, from the anticipation of meandering. From Figure 6, it seems that the wake breakdown is triggered by destabilization of the
270 hub vortex, which would be consistent with some of the literature (Iungo et al., 2013). To quantify the gains obtained by using the helix, we first looked at the global quantities for the rotor. The turbine's power output is reduced as expected since the pitch signal is suboptimal. The maximum power loss with respect to the baseline is 3.66%. This is reported in Table 6. From Table 6 we can also observe that the loss decreases as the excitation frequency increases.

However, the helix should allow downstream turbines to compensate for the loss and increase the power at a farm level.
275 Other studies on DIC were performed considering downstream turbines as sensors to assess the effect on the wake. Since
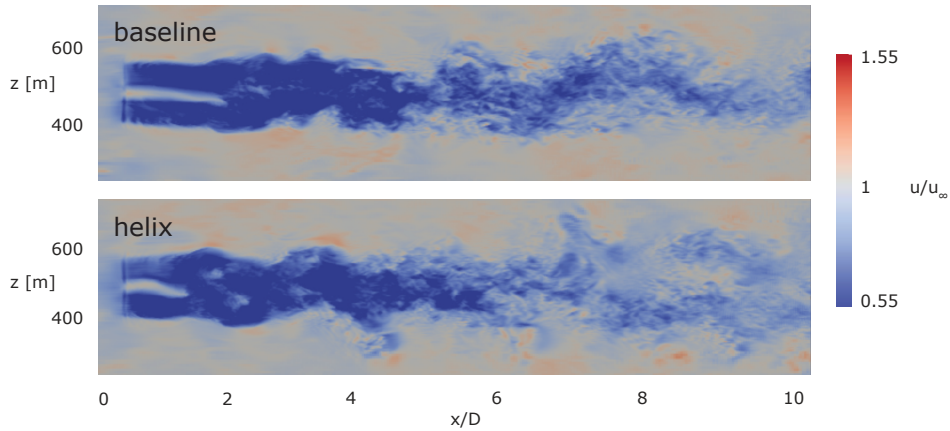
Figure 5. Horizontal snapshot of the stream-wise velocity component (u) at the final time step for baseline control (top) and for the helix with excitation St 0.4 (bottom). Turbulence intensity in both cases is 3.3%
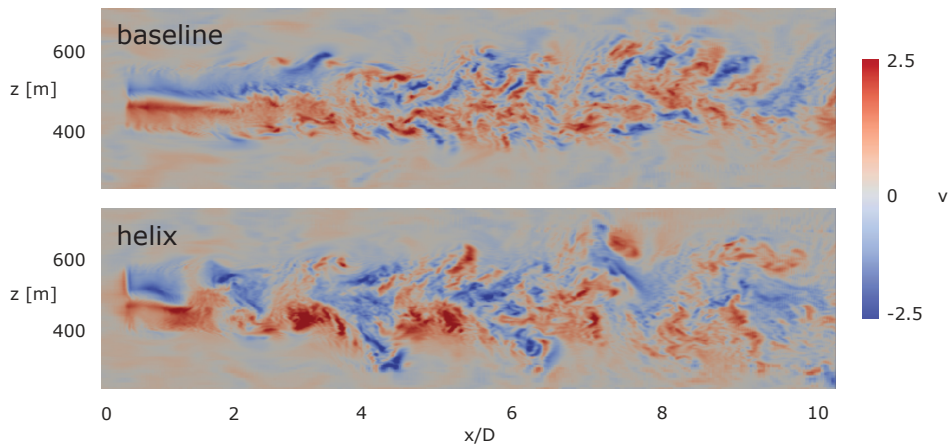
Figure 6. Horizontal snapshot of the vertical velocity component (v) at the final time step for baseline control (top) and for the helix with excitation St 0.4 (bottom). Turbulence intensity in both cases is 3.3%

we have only one turbine in our simulations, we introduced some "ghost" turbines. We selected planes at multiple distances downstream of the turbine and looked at what kind of inflow would be available to a turbine of the same diameter aligned with it. To do so, we considered the mean velocity on each point of the plane contained in a circle with the same diameter as the turbine, averaged it in space, and elevated it to the power of three. We will refer to this quantity as "power available" because, for the scope of our analysis, we are interested in trends and ratios and don't need an exact value.

Figure 7 shows the power available at the different considered locations for the baseline case compared to the helix cases at different Strohual numbers, normalized by the rotor power for the baseline case. For uniform inflow, the further downstream we move, the more effective the helix proves in recovering energy. In the range $St \in [0.3 - 0.4]$ the lines come closer together with

Table 6. Turbine power variations obtained with the helix with different inflow conditions with respect to the baseline case value corresponding with the same inflow.

	Rotor Power					
	$St = 0.15$	$St = 0.2$	$St = 0.25$	$St = 0.3$	$St = 0.35$	$St = 0.4$
Uniform Inflow	-3.66 %	-3.16%	-2.71%	-2.32%	-2.04%	-1,67%
TI=3.3 %	-3.24%	-3.22%	-2.95%	-2.7%	-2.34%	-2.16 %
TI=6.5 %	-3,58%	-3.21%	-2.94%	-2.79%	-2.58%	-2.38%
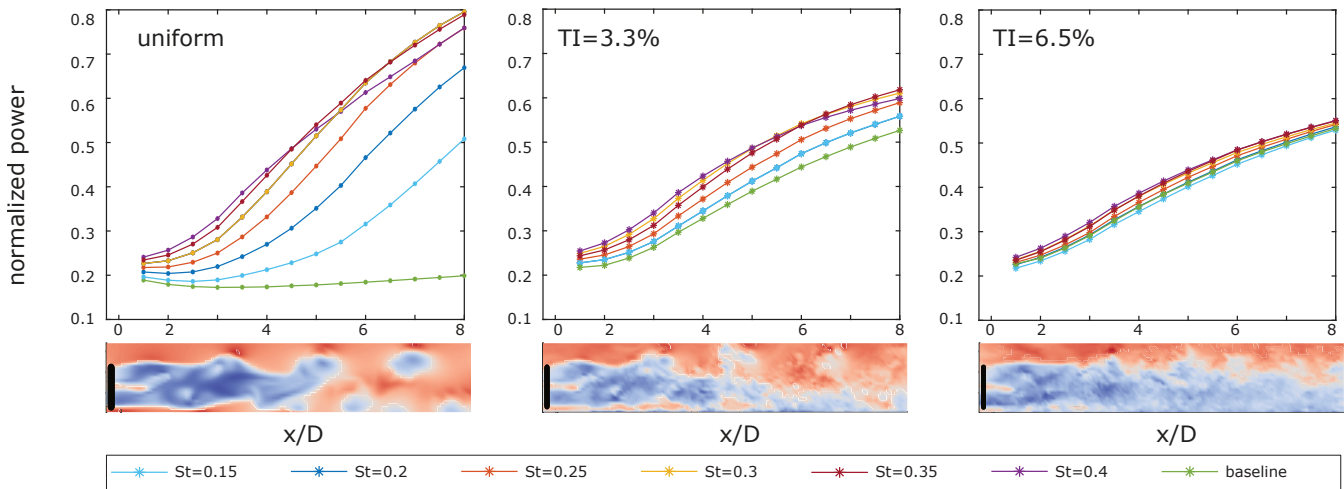
Figure 7. Available power estimate at different locations downstream of the rotor for all cases. From left to right, we show the uniform case, the low turbulence intensity case, and the high turbulence intensity case. Underneath the plots, we show vertical slices of stream-wise velocity from the case with $St = 0.4$ for illustrative purposes.

the optimum recovery depending strongly on the position after about four and a half diameters downstream. With turbulent

285 inflow, the advantage obtained in the near-wake is more or less retained until the end of our sampling box. The observation on the gain saturation in the range $St \in [0.3 - 0.4]$ remains true for the low turbulence intensity case.

In the uniform inflow case, the gains are much higher, which was expected since, in the other cases, the most important factor in the recovery is the inflow turbulence. However, the gains obtained in the turbulent cases when using the helix would be very significant in a real wind farm scenario. One general conclusion can be drawn from this analysis: the optimal Strohual

290 number for the helicoidal excitation depends on both the turbulence intensity and the position downstream.

The slices in Figure 8 are parallel to the rotor plane and show the mean stream-wise velocity at the "ghost" turbines positions at $St_{exc} = 0.4$. We can observe how the flow evolves depending on the inflow: the stream-wise velocity outside of the rotor area is higher than the free-stream for the turbulent cases because the inflow profile is such that the free-stream value is imposed

only at hub height. In the near-wake, the closer we are to the wake center, the higher the deficit. At a distance of 6 and 8 diameters downstream of the turbine, that area presents a higher stream-wise velocity for the uniform case.
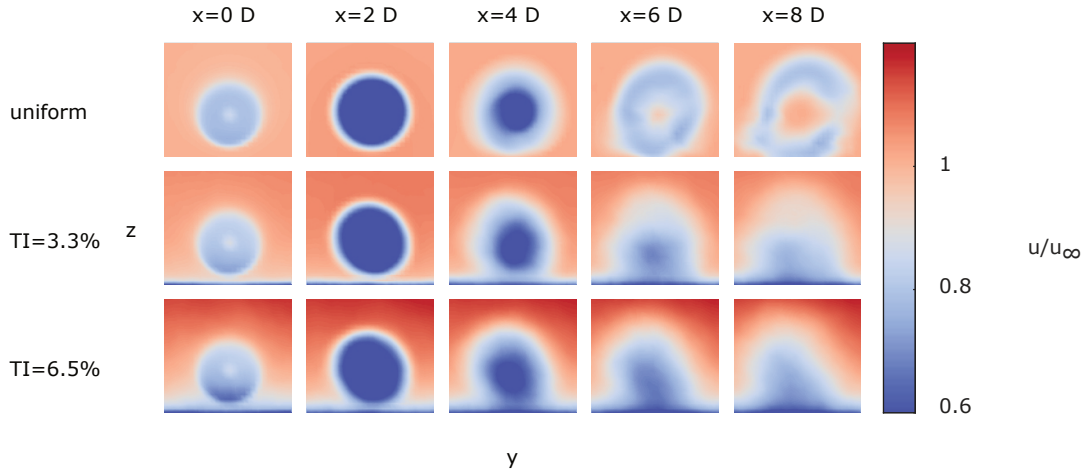
Figure 8. Mean stream-wise velocity immediately downstream of the rotor plane and at parallel planes at various distances downstream for all inflow conditions and $St_{exc} = 0.4$.

295

4.2 Dynamic mode decomposition analysis

The data structure obtained from the simulations has dimensions of $96000 \times 800 \times 3$. The first dimension is space, the second is time, and then, for each spatio-temporal coordinate, we have collected all three velocity components. This choice of observables is the same as in Muscari et al. (2023). What was found, in that case was that the results where the same with the three velocity

300 components or with the stream-wise only (because of the uniform horizontal inflow), but spurious modes appeared when also considering the pressure. We reorganized the data in column vectors that we feed to the DMD algorithm.

4.2.1 Uniform case

The selected rank for our decomposition is $r = 15$. This results in seven modes. One mode always has zero frequency and is representative of the mean flow. In the following, we will call this mode M. We evaluated the model accuracy by computing

305 the relative root mean square error (RRMSE) in the range $r \in [1, 181]$ as shown in Figure 9.

The RRMSE is a normalized measure of the differences between values predicted by a model and the measurements. In our case, it is calculated based on the element-wise residuals between the true snapshot matrix $\mathbf{X}'$ and its reconstruction $\mathbf{X}'_{DMD,ij}$:

$$RRMSE = \sqrt{\frac{\frac{1}{nm}\sum_{i=1}^{n}\sum_{j=1}^{m}(\mathbf{X}'_{ij} - \mathbf{X}'_{DMD,ij})^2}{\sum_{i=1}^{n}\sum_{j=1}^{m}(\mathbf{X}'_{ij})^2}} \tag{14}$$
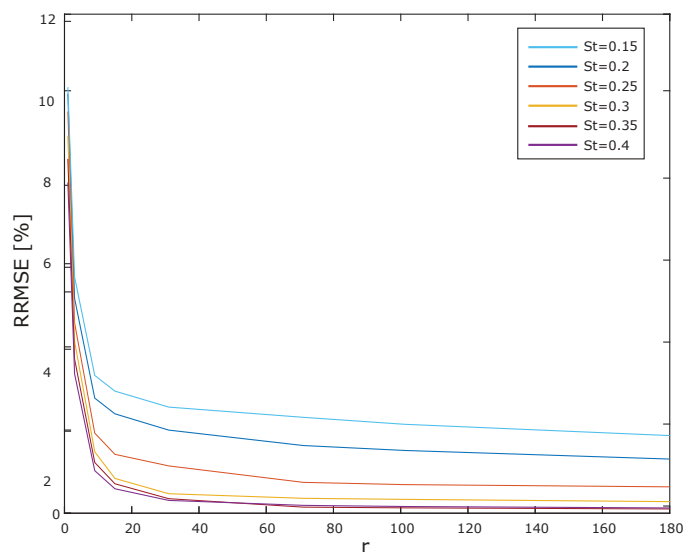
Figure 9. Relative root mean square error when modeling the flow with DMD as a function of the chosen rank. Different lines represent different Strouhal numbers of the excitation signal.

310

We see that the error strongly depends on the excitation. This is because, since the helix is more effective at higher frequencies, the helicoidal modes, whatever the rank, retain more energy content that would otherwise be more widely distributed.

Frequencies and amplitudes of the uniform inflow complex conjugate modes are represented in Figure 10. The first and
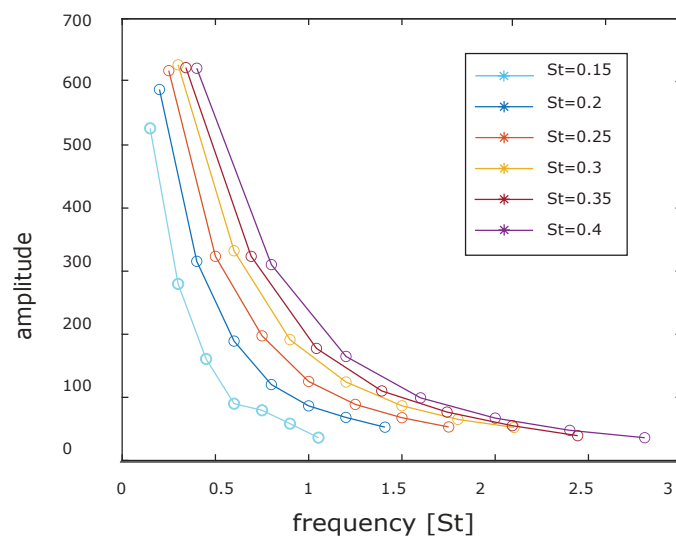
Figure 10. Spectral representation of the modes for all the uniform inflow helix cases.

most important mode always has the same frequency as the imposed helix signal. The other modes have frequencies that are
harmonics of the first. In the following, we will be indicating these modes as H_1 for the first helix modes and H_n for the
harmonics (where n is the relative integer multiple). The amplitude can be related to the total energy content in the considered
volume. As seen in Section 4.1, the optimum Strouhal also depends on the stream-wise position. Figure 11 shows iso-surfaces
of the stream-wise velocity component reconstructed from the first three helix modes. The iso-values for Figure 11 are chosen
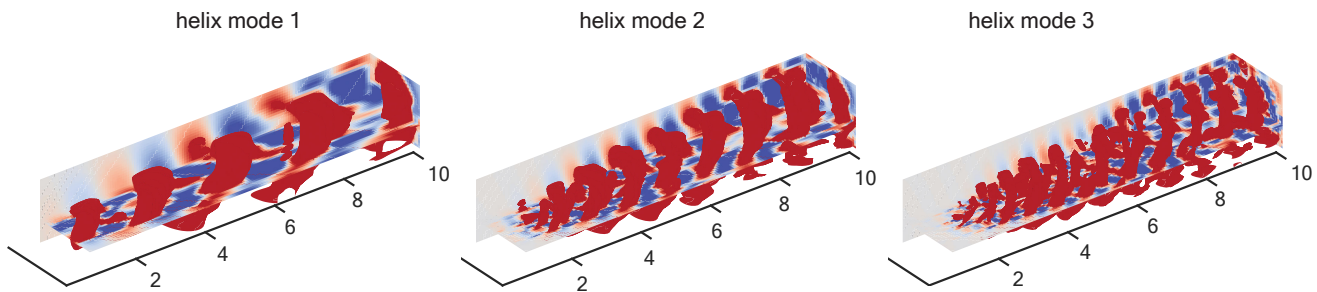
Figure 11. Iso-surfaces of the stream-wise velocity component reconstructed from modes H_1, H_2, and H_3 (from left to right). The free-stream velocity was 9 m/s. Three slices, positioned at the left, bottom, and downstream boundaries of the domain, are added to improve visualization.

so that they give a good visual representation of the mode, and they are different for the different modes. We of course
recognize the helicoidal pattern and evidence how, together with harmonic growing of the frequency, the structures become
closer together. Figure 12 gives us an idea of the reconstruction quality obtainable with just the mean and the first helix mode
in the uniform case.
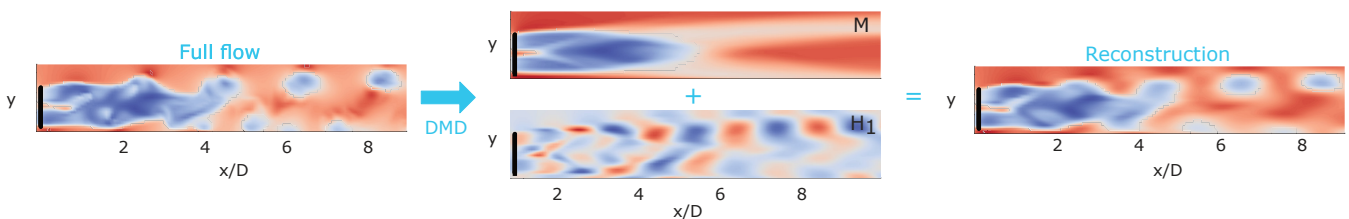
Figure 12. Representation of the reconstruction obtained with only mode 0 and more 1 for the uniform case with $St = 0.4$.

The information conveyed by Figure 12 can be quantified using the same criterion chosen to select the DMD rank. With
the rank being fixed to 15, we evaluated the error using different modes for reconstruction. Figure 13 shows the results of this
evaluation.
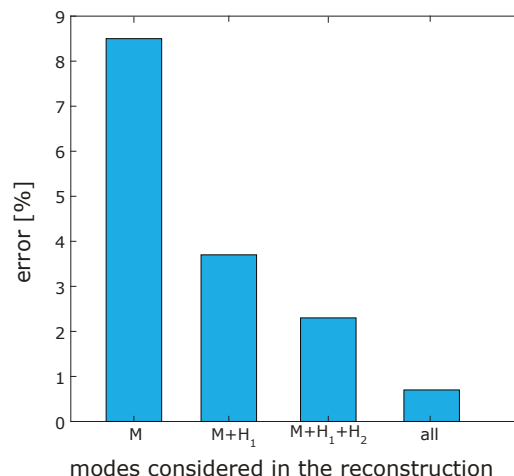
Figure 13. Relative root mean square error when modeling the flow with DMD with only selected modes. Mode 0 (M) is always present since it represents the mean.

4.2.2 Turbulent case

In this section, we finally address the two main research questions: do helix modes still show up in low-rank DMD of a turbulent inflow wake? Can we establish if the helix triggers wake meandering as inflow perturbations with similar frequencies did in Mao and Sørensen (2018) and Li et al. (2022)?

330   In turbulent cases, as expected, the quality of the reconstruction is lower. The energy associated with the complex modes is several orders of magnitude lower than the one associated with mode 0. This does not mean the helicoidal mode cannot contribute significantly to the dynamics. Given an excitation frequency, the error remains constant in the range of ranks tested for the uniform case $r \in [1, 181]$. The error varies from a minimum of 7.6% for $St = 0.4$ to a maximum of 8.1% for $St = 0.2$. For consistency with the uniform case, we picked $r = 15$ again.

335   To isolate the effect of turbulence, we first performed DMD on the precursor simulations. Because of the coarser mesh, the data structure is considerably smaller, namely $96000 \times 300 \times 3$.

For both precursors, the dominant frequency ($St = 0.072$) is related to the vertical integral length scale found for the precursors, as shown in Section 3.3. The other dominant frequencies are the first and second harmonic. In the following, as done for the helix modes, we will refer to these modes as I_1 for the first inflow mode and I_n for the harmonics (where n is the relative

340   integer multiple). The frequency related to the stream-wise integral length scale is also present but is not dominant. These modes are still relevant for the successors: we find them again in addition to the helix-related modes. Although we expected to find the precursor modes (we already know that turbulence dominates the flow field), whether the helix modes would still be relevant was an open question. From figure 14, we can observe how the turbulence intensity modifies the amplitude of the modes and their spacial decay but not their frequencies.
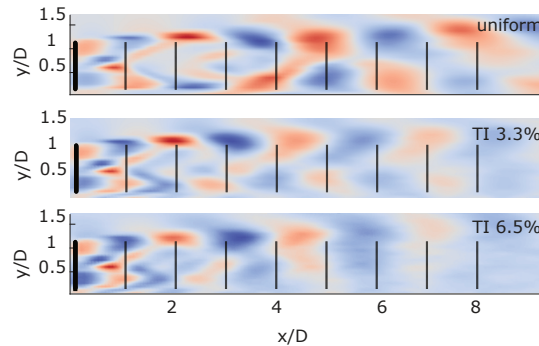
Figure 14. Vertical slices of the stream-wise velocity component, reconstructed from the first helix mode for the uniform case and the two turbulent cases with $St_{exc} = 0.3$. The frequency of this mode is also $St = 0.3$.

345   In general, the exact DMD modes follow a predictable pattern for turbulent cases, given an excitation frequency and the precursor characteristics. One or more zero frequency modes over which the mean flow is distributed, one mode at the dominant precursor frequency with some of its harmonics (inflow modes), and one mode at the excitation frequency with some of its harmonics (helix modes).

     Figures 15 and 16 show the flow reconstruction obtainable with only the mean flow and the helix mode for the case with
350     $St = 0.4$ at both turbulence intensities. As already mentioned, the quality is significantly lower with respect to the uniform case (See Figure 12), but the first helix mode is still dominating the dynamics. Any attempt at reconstructing the full flow that does not include it is indistinguishable from the mean.
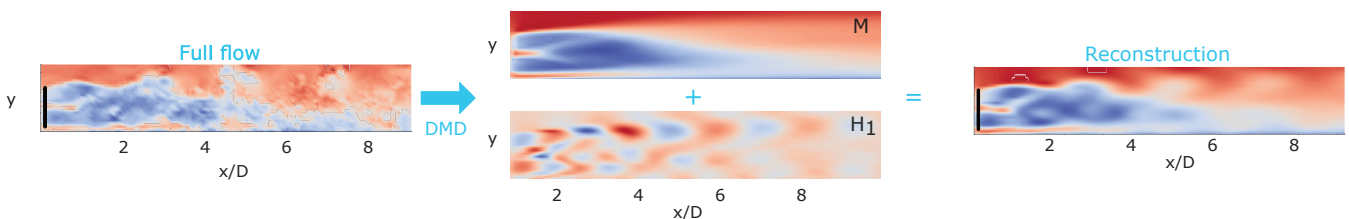
Figure 15. Representation of the reconstruction obtained with only mode 0 and the first helix mode for the case with $St = 0.4$ and $TI = 3.3\%$.

     The information conveyed by Figure 15 and Figure 16 can be quantified using the same criterion chosen to select the DMD rank. With the rank being fixed to 15, we evaluated the error using different modes for reconstruction. Figure 17 shows the
355   results of this evaluation.
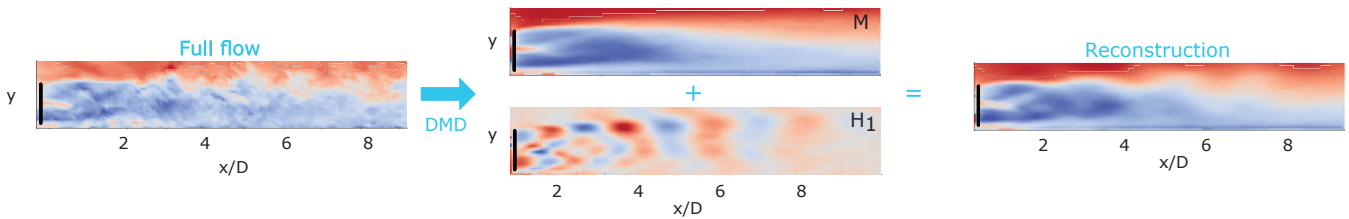
Figure 16. Representation of the reconstruction obtained with only mode 0 and the first helix mode for the case with $St = 0.4$ and $TI = 6.5\%$.
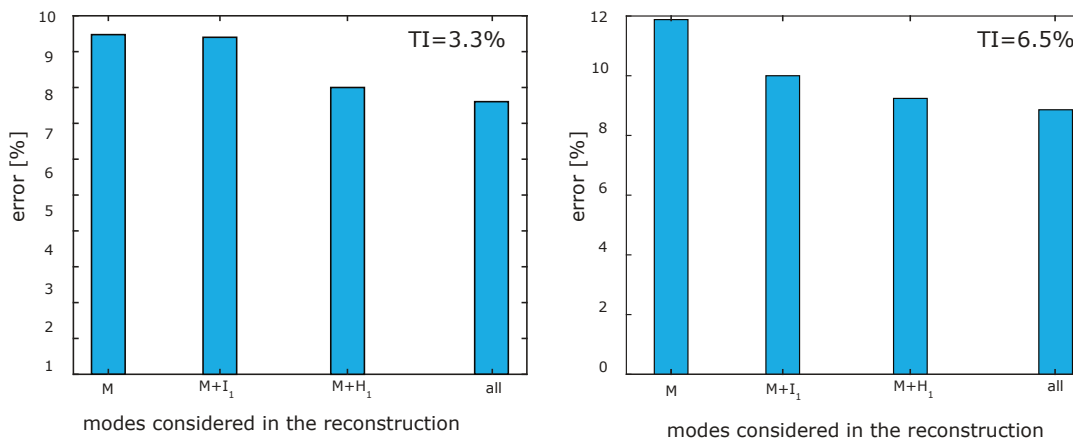
Figure 17. Relative root mean square error for the turbulent cases with $St = 0.4$ when modeling the flow with DMD with only selected modes. Mode 0 (M) is always present since it represents the mean.

5 Conclusions

In this paper, we reported the results of a numerical study that characterized the dynamic response of wakes manipulated with DIC techniques. The considered turbine was the DTU 10 MW. Its operation under three different inflow conditions was simulated using the CFD framework SOWFA with the blades modeled as actuator lines.

360   The main finding of this study is that the helix retains its dynamic importance when a realistic value of turbulence intensity is considered. Analysing the data via an exact DMD algorithm, we retrieved the eight most relevant dynamic modes associated with the wake. The helix modes are still dominant. We found that the frequencies of dominant modes are associated with the turbulent length scales of the inflow and with the pitch excitation. The turbulence intensity affects their amplitudes and spatial decay. Wake energy content analysis at various downstream locations also led to an important finding: the optimal St_{exc} for

365   the helix varies with the turbulence intensity and the downstream position.

     The found optimal St values are consistent with the observation in Hodgson et al. (2023) that inflow Strouhal numbers in the range of $St = 0.33$ to $St = 0.66$ results in optimal amplification of stream-wise velocity fluctuations, but, with the current simulation setup, there is no clear relationship between the excitation frequency and the triggering of meandering as in Mao

and Sørensen (2018) and Li et al. (2022). The modes obtained from DMD also give us a simple, linear, model the helicoidal wake. We show that a fair reproduction of the full-flow dynamics is not attainable without the first helix mode and that, in a turbulent case, a simple wake model that only takes into account the rigid mode (mean flow) and the first helix mode, which is an order reduction from infinite to two, leads to a maximum error of 3% on the reconstruction of the full flow field for uniform inflow case, and a maximum of 9% for the turbulent ones. The percentages given for the turbulent cases refer to the case with $St_{exc} = 0.4$, but we don't expect big variations with St_{exc}. In the uniform case, the reconstruction error is generally much lower and more dependent on the rank of the initial decomposition and on St_{exc}.

Our recommendation for future work is to augment the space and time resolution to the point where the influence of tip vortices and their interaction with the hub vortex can be assessed. Moreover, the modes' dependency on other inflow parameters (such as turbulence length scales) needs to be assessed.

Code and data availability. Code and data will be made available on request.

Author contributions. **C. Muscari**: Formal analysis, Investigation, Data curation, Writing; **P. Schito**: Resources, Supervision; **A. Viré**: Resources, Supervision; **A. Zasso**: Resources, Supervision; **JW van Wingerden**: Conceptualization, Resources, Supervision.

Competing interests. At least one of the (co-)authors is a member of the editorial board of Wind Energy Science.

References

Akhmatov, V. and Knudsen, H.: An aggregate model of a grid-connected, large-scale, offshore wind farm for power stability investiga-
385   tions—importance of windmill mechanical system, International Journal of Electrical Power & Energy Systems, 24, 709–717, 2002.

Alla, A. and Kutz, J. N.: Nonlinear model order reduction via dynamic mode decomposition, SIAM Journal on Scientific Computing, 39,
B778–B796, 2017.

Bak, C., Zahle, F., Bitsche, R., Kim, T., Yde, A., Henriksen, L. C., Hansen, M. H., Blasques, J. P. A. A., Gaunaa, M., and Natarajan, A.: The
DTU 10-MW reference wind turbine, in: Danish wind power research 2013, 2013.

390   Campagnolo, F., Weber, R., Schreiber, J., and Bottasso, C. L.: Wind tunnel testing of wake steering with dynamic wind direction changes,
Wind Energy Science, 5, 1273–1295, 2020.

Cassamo, N. and van Wingerden, J.-W.: Model predictive control for wake redirection in wind farms: a koopman dynamic mode decompo-
sition approach, in: 2021 American Control Conference (ACC), pp. 1776–1782, IEEE, 2021.

Churchfield, M., Lee, S., and Moriarty, P.: Overview of the simulator for wind farm application (SOWFA), National Renewable Energy
395   Laboratory, 2012a.

Churchfield, M. J., Lee, S., Michalakes, J., and Moriarty, P. J.: A numerical study of the effects of atmospheric and wake turbulence on wind
turbine dynamics, Journal of turbulence, p. N14, 2012b.

Clayton, B. and Filby, P.: Measured effects of oblique flows and change in blade pitch angle on performance and wake development of model
wind turbines, in: Proc 4th BWEA Wind Energy Conference, 1982.

400   Croce, A., Cacciola, S., Montero Montenegro, M., Stipa, S., and Praticó, R.: A CFD-based analysis of dynamic induction techniques for
wind farm control applications, Wind Energy, 26, 325–343, 2023.

Doekemeijer, B. M., Kern, S., Maturu, S., Kanev, S., Salbert, B., Schreiber, J., Campagnolo, F., Bottasso, C. L., Schuler, S., Wilts, F., et al.:
Field experiment for open-loop yaw-based wake steering at a commercial onshore wind farm in Italy, Wind Energy Science, 6, 159–176,
2021.

405   Fleming, P., Gebraad, P., van Wingerden, J.-W., Lee, S., Churchfield, M., Scholbrock, A., Michalakes, J., Johnson, K., and Moriarty, P.:
SOWFA super-controller: A high-fidelity tool for evaluating wind plant control approaches, Tech. rep., National Renewable Energy
Lab.(NREL), Golden, CO (United States), 2013.

Fleming, P., Gebraad, P. M., Lee, S., van Wingerden, J.-W., Johnson, K., Churchfield, M., Michalakes, J., Spalart, P., and Moriarty, P.:
Simulation comparison of wake mitigation control strategies for a two-turbine case, Wind Energy, 18, 2135–2143, 2015.

410   Frederik, J., Doekemeijer, B., SP, M., and van Wingerden JW: The helix approach: Using dynamic individual pitch control to enhance wake
mixing in wind farms, Wind Energy, 23, 1739–1751, 2020.

Gebraad, P. M., Teeuwisse, F. W., Van Wingerden, J., Fleming, P. A., Ruben, S. D., Marden, J. R., and Pao, L. Y.: Wind plant power
optimization through yaw control using a parametric model for wake effects—a CFD simulation study, Wind Energy, 19, 95–114, 2016.

Glauert, H.: Aerodynamic Theory: A General Review of Progress, volume IV, chapter Division L, Airplane Propellers, 1963.

415   Greenshields, C. J. et al.: Openfoam user guide version 6, The OpenFOAM Foundation, 237, 624, 2018.

Hodgkin, A., Deskos, G., and Laizet, S.: On the interaction of a wind turbine wake with a conventionally neutral atmospheric boundary layer,
International Journal of Heat and Fluid Flow, 102, 109 165, 2023.

Hodgson, E. L., Madsen, M. H. A., and Andersen, S. J.: Effects of turbulent inflow time scales on wind turbine wake behavior and recovery,
Physics of Fluids, 35, 2023.

420 IEA, P.: IEA Report 2023, World Energy Outlook 2023, Tech. rep., IEA, 2023.

Iungo, G. V., Viola, F., Camarri, S., Porté-Agel, F., and Gallaire, F.: Linear stability analysis of wind turbine wakes performed on wind tunnel measurements, Journal of Fluid Mechanics, 737, 499–526, 2013.

Jasak, H.: OpenFOAM: Open source CFD in research and industry, International journal of naval architecture and ocean engineering, 1, 89–94, 2009.

425 Jiménez, Á., Crespo, A., and Migoya, E.: Application of a LES technique to characterize the wake deflection of a wind turbine in yaw, Wind energy, 13, 559–572, 2010.

J.L., L.: The structure of inhomogeneous turbulent flows, Atmospheric turbulence and radio wave propagation, 1967.

Jonkman, J., Butterfield, S., Musial, W., and Scott, G.: Definition of a 5-MW reference wind turbine for offshore system development, Tech. rep., National Renewable Energy Lab.(NREL), Golden, CO (United States), 2009.

430 Korb, H., Asmuth, H., and Ivanell, S.: The characteristics of helically deflected wind turbine wakes, Journal of Fluid Mechanics, 965, A2, 2023.

Larsen, G. C., Madsen, H. A., Thomsen, K., and Larsen, T. J.: Wake meandering: a pragmatic approach, Wind Energy: An International Journal for Progress and Applications in Wind Power Conversion Technology, 11, 377–395, 2008.

Lee, S., Churchfield, M., Moriarty, P., Jonkman, J., and Michalakes, J.: Atmospheric and wake turbulence impacts on wind turbine fatigue
435 loadings, in: 50th AIAA Aerospace Sciences Meeting including the New Horizons Forum and Aerospace Exposition, p. 540, 2012.

Li, Z., Dong, G., and Yang, X.: Onset of wake meandering for a floating offshore wind turbine under side-to-side motion, Journal of Fluid Mechanics, 934, A29, 2022.

Lin, M. and Porté-Agel, F.: Wake meandering of wind turbines under dynamic yaw control and impacts on power and fatigue, Renewable Energy, p. 120003, 2024.

440 Magionesi, F., Dubbioso, G., Muscari, R., and Di Mascio, A.: Modal analysis of the wake past a marine propeller, Journal of Fluid Mechanics, 855, 469–502, 2018.

Mao, X. and Sørensen, J.: Far-wake meandering induced by atmospheric eddies in flow past a wind turbine, Journal of Fluid Mechanics, 846, 190–209, 2018.

Meyers, J., Bottasso, C., Dykes, K., Fleming, P., Gebraad, P., Giebel, G., Göçmen, T., and Van Wingerden, J.-W.: Wind farm flow control:
445 prospects and challenges, Wind Energy Science, 7, 2271–2306, 2022.

Munters, W. and Meyers, J.: Towards practical dynamic induction control of wind farms: analysis of optimally controlled wind-farm boundary layers and sinusoidal induction control of first-row turbines, Wind Energy Science, 3, 409–425, 2018.

Muscari, C., Schito, P., Viré, A., Zasso, A., Van Der Hoek, D., and Van Wingerden, J.: Physics informed DMD for periodic dynamic induction control of wind farms, in: Journal of Physics: Conference Series, vol. 2265, p. 022057, IOP Publishing, 2022.

450 Muscari, C., Schito, P., Viré, A., Zasso, A., and van Wingerden, J.-W.: Physics-informed data-driven reduced-order models for Dynamic Induction Control, IFAC-PapersOnLine, 56, 8414–8419, 2023.

Rodi, W., Ferziger, J. H., Breuer, M., Pourquié, M., et al.: Status of large eddy simulation: results of a workshop, Transactions-American Society of Mechanical Engineers Journal of Fluids Engineering, 119, 248–262, 1997.

Rowley, C. W., Mezić, I., Bagheri, S., Schlatter, P., and Henningson, D. S.: Spectral analysis of nonlinear flows, Journal of fluid mechanics,
455 641, 115–127, 2009.

Sarmast, S., Dadfar, R., Mikkelsen, R. F., Schlatter, P., Ivanell, S., Sørensen, J. N., and Henningson, D. S.: Mutual inductance instability of the tip vortices behind a wind turbine, Journal of Fluid Mechanics, 755, 705–731, 2014.

Schmid, P. J.: Dynamic mode decomposition of numerical and experimental data, Journal of fluid mechanics, 656, 5–28, 2010.

Schmid, P. J.: Dynamic mode decomposition and its variants, Annual Review of Fluid Mechanics, 54, 225–254, 2022.

460 Siemens Gamesa: Siemens Gamesa now able to actively dictate wind flow at offshore wind locations, https://www.siemensgamesa.com/en-int/newsroom/2019/11/191126-siemens-gamesa-wake-adapt-en, accessed: 2018-12-06, 2019.

Sorensen, J. N. and Shen, W. Z.: Numerical modeling of wind turbine wakes, J. Fluids Eng., 124, 393–399, 2002.

Tu, J. H.: Dynamic mode decomposition: Theory and applications, Ph.D. thesis, Princeton University, 2013.